PAUL SCHERRER INSTITUT		Registrierung TM-35-08-01
Titel	A new detector system for the ALC spectrometer -- first experience with G-APDs in μSR instrumentation	Ersetzt
Autoren / Autorinnen	A. Stoykov, R. Scheuermann, K. Sedlak, T. Shiroka, V. Zhuk *	Erstellt 05.03.2008

Zusammenfassung:

The development and performance of a new detector system for the Avoided Level Crossing (ALC) μSR-spectrometer, located at the Swiss Muon Source of the Paul Scherrer Institut, are presented.

The distinctive feature of the new ALC-detector is the absence of such conventional components as photomultiplier tubes and light guides. Their functions are taken over by Geiger-mode Avalanche Photodiodes (G-APDs) and wavelength-shifting fibers. This approach allows us to build a compact, magnetic field insensitive detector, requiring low operation voltage.

* Joint Institute for Nuclear Research, 141980 Dubna, Moscow region, Russia

Verteiler

Abt.	Empfänger / Empfängerinnen	Expl.	Abt.	Empfänger / Empfängerinnen	Expl.
3501	A. Amato	1			
3000	R. Bercher	3			
3000	K. Clausen	1			
8580	K. Deiters	1			
3500	D. Herlach	1			
3502	E. Morenzoni	1			
3502	T. Prokscha	1			
1412	D. Renker	1			
1414	N. Schlumpf	1			

	Expl.
Bibliothek	3
Reserve	3
Total	17
Seiten	19
Beilagen	
Informationsliste	
D 1 2 3 4 5 8 9 A	
Visum Abt.-/Laborleitung:	

1 Introduction

The Avoided Level Crossing (ALC) spectrometer [1] at the Swiss Muon Source (SμS) of the Paul Scherrer Institut (PSI, Villigen, Switzerland) is used to study the properties of condensed matter via the observation of the loss of integrated muon spin polarization at the avoided crossing of quantized magnetic energy levels in high magnetic fields [2].

Figure 1 shows the ALC spectrometer in the experimental area πE3 of SμS as it has been set up during the past years. The basic part of the spectrometer is a superconducting solenoid with a room–temperature bore of 20 cm in diameter and a length of 1 m, which creates a longitudinal (with respect to the initial muon spin polarization) magnetic field up to 5 Tesla at its center. A sample, mounted in a cryostat, is positioned in the center of the solenoid warm bore. The positrons arising from the decay of muons stopped in the sample are detected by two sets of segmented scintillation counters, as schematically shown in Fig. 2a. The backward positron detector (BW) has a *cylindrical* shape and is made of 8 identical segments. The forward detector (FW) consists of 7 triangular segments, which form a *disc*, positioned perpendicular to the beam behind the cryostat (one counter, out of 8, is removed to make space for the cryostat mounting). One of the backward counters can be optionally replaced by a muon counter thus allowing for time-differential operation. The muon counter is not used in the ALC mode.

The scintillators are readout by photomultiplier tubes placed sufficiently far from the magnet to minimize the effect of the stray magnetic field on their performance. The scintillation light is transported to the PMTs by long bended light guides and thus gets substantially attenuated. The overall construction of the detector system is quite bulky and rigid, limiting therefore any flexibility in the detector geometry.

The spectrometer is operated in a time-integral mode. The integral counts in backward N_{B} and forward N_{F} detectors are measured as a function of the magnetic field H. The asymmetry A is calculated as:

$$A = \frac{N_{\mathrm{B}} - N_{\mathrm{F}}}{N_{\mathrm{B}} + N_{\mathrm{F}}} \ . \tag{1}$$

A loss of the integral muon-spin polarization at resonance values of the magnetic field results in a decrease (increase) in the number of counts in backward (forward) detectors and is detected as a dip in the field dependence of the asymmetry (the ALC resonance [2]). The complexity of the analysis of the ALC resonances will strongly depend on the field dependence of the asymmetry baseline (by asymmetry baseline we designate the $A(H)$ curve in the absence of resonances). Hence a straightforward analysis of the resonances often requires a simple shape and gentle slope of the asymmetry baseline.

However, in any practical realization of the ALC setup the effective solid angle of the detectors and, accordingly, the asymmetry baseline vary with the field due to: a) variation of the efficiencies of the detectors (gain variation of PMTs); b) movement and oscillations of the muon beam spot [3]; c) field-dependent positron trajectories. The goal of the present work is to construct a detector system in which the effect of the above factors on the ALC data quality is minimized.

For the new ALC detector setup we have chosen a two-ring configuration as shown in Fig. 2b. GEANT4 [4, 5] simulations (details will be given in a separate publication) indicate that for such a detector layout the decrease of the effective solid angle of the BW detector with increasing H can be, to a certain extent, compensated by a similar decrease of the effective solid angle of the FW detector thus reducing the slope of the asymmetry baseline (see Fig. 3). Simulations suggest that the effect of the field on the asymmetry

is minimum if: a) the gap between the detectors and the sample is minimized, i.e their effective solid angle is maximum at $\mu_0 H = 0$ T; b) the energy losses of the decay positrons in the sample are sufficiently small; c) there are no gaps in the detector rings – all the segments are present and have the same, close to 100 %, efficiency; d) the diameters of the BW and FW rings are as small as possible (this requirement is, of course, in contradiction with the necessity to have a high rate of muons stopped in the sample).

Other benefits of the two-ring detector configuration are: a) the possibility to use a standard, axially symmetric cryostat; b) the higher performance stability: the FW detector stays out of the beam and therefore is much less sensitive to its contamination with positrons, which might fluctuate, for example, due to an unstable operation of the separator.

For the detector realization we have chosen a technology based on G-APDs instead of PMTs. The potential of G-APD based detectors for the development of μSR techniques has already been discussed in [6]. This choice gives us the following advantages:

- compact size of the detector and its insensitivity to the magnetic field;
- higher flexibility in detector design and more possibilities for optimization;
- low operation voltage.

2 The new ALC detector

2.1 Design

Figure 4 shows the mounting of the detector module in the solenoid. The annular Pb-shield at the entrance of the solenoid protects the counters from the background coming from the beamline. Two lead collimators inside the extension tube decrease the final beam down to a diameter of 33 mm. A cryostat, to be implemented in the next stage of the spectrometer upgrade, is presently substituted by a sample holder. Note, that the front part of the sample holder is a hollow cylinder, rather than a central rod. This form is adopted in order to minimize the effective thickness of the sample and to avoid the modulation of this parameter caused by the oscillations of the muon beam spot size.

The detector module, see Fig. 5, is a standalone construction. It can therefore be assembled separately and then, as a whole, mounted in its proper place inside the solenoid. It consists of two rings holding ten detector segments. The standard detector segment hosts two positron counters. One of these segments can be replaced by a segment holding one positron and one muon counters – in this configuration one gets the possibility to perform time differential μSR measurements. To make the handling of the detector module easier, all the signal and power cables coming from the counters are terminated to connectors within the module.

The positron counter (Fig. 6) is based on a scintillator tile containing two grooves into which wavelength shifting (WLS) fibers are glued. The light emitted in the scintillator is collected by the fibers, re-emitted and subsequently transported to the photosensors – a pair of G-APDs connected in series. Additional amplification of the detector signal is done by an amplifier inside the detector module.

The muon counter (Fig. 7) is realized in a similar way: the light from a thin (300 μm) plastic scintillator is collected first by a plexiglass ring and then by a WLS fiber glued into a groove made in the ring. The light trapped in the fiber is then transported to a G-APD.

Table 1: The parameters of G-APDs as given in the data sheets of the companies Photonique SA and Hamamatsu. Data from [11], [12], and our estimates are indicated as (*), (**), and (***), respectively. Since the G-APD parameters depend on the operating conditions (bias voltage) the given values are indicative.

G-APD	SSPM-0701BG	MPPC-S10362-11-050C
Active area, mm^2	1	1
Number of cells	560	400
Operating voltage, V	~ 20	~ 70
PDE at 490 nm, %	30	40 (30*)
Gain	$\leq 4 \cdot 10^5$	$\leq 10^6$
Temperature coefficient of Gain, $\%/C^o$	0.7	7
Cell recovery time, ns	–	10**
Dark count, MHz	7***	0.3
Inter-cell crosstalk, %	< 20	< 20*

2.2 Implementation

The detector module, positron and muon counters are shown in Fig. 8 and 9. Figure 10 shows the scheme and the board of the amplifier used in both types of counters. Voltage regulator modules [7] are used for biasing the G-APDs. Figure 11 exhibits a crate with three of these modules (24 channels).

For the positron counters we use G-APDs of type SSPM-0701BG produced by Photonique SA [8]. The main criteria for this choice were a high photon detection efficiency *PDE* as well as the very weak temperature dependence of the gain (see Tab. 1). The temperature stability is an essential requirement to ensure a constant efficiency of the counters throughout variations of the ambient temperature: any change in efficiency would alter the asymmetry baseline.

For the muon counter we use a G-APD of type MPPC-S10362-11-050C produced by Hamamatsu [9]. Since the muon counter is used only in the time-differential mode of operation, the temperature dependence of its response is not a central issue. A more important requirement in this case, along with the high *PDE*, appears to be a low rate of dark 1e - signals from the avalanche breakdown of single G-APD cells triggered by thermally generated charge carriers. The dark count rates of different G-APDs at room temperature vary in the range $10^5 - 10^7$ $s^{-1}mm^{-2}$ with a detection threshold set at $0.5A_{1e}$ (A_{1e} is the amplitude of the 1e - signals). Taking into account the inter-cell crosstalk one has to increase the detection threshold to keep the dark count rate low. The necessity to set trigger threshold levels well above A_{1e} decreases the signal-to-threshold (signal-to-noise) ratio of the G-APD based scintillation counters and is critical for the detection of low level light signals (in our case the amount of light collected from the thin scintillator of the muon counter is expected to be much smaller [10] compared to that from the thicker positron counter).

The signals from all 20 counters are transported by $\sim$ 50 m long low-loss cables to a data acquisition system. Constant fraction discriminators PSI CFD-950 are used to receive and shape the signals. The shaped signals from BW and FW positron counters are summed by two OR-logic units and then sent to scalers. During an ALC experiment, for each set value of the magnetic field the scalers are run over a predefined time interval (typically $10 - 20$ s, depending on the intensity of the proton beam) to obtain the integral

counts N_B and N_F, which are then used to calculate the asymmetry. Note, that N_B and N_F are hardware corrected for double hits, i.e. each positron hitting several detectors is counted once. The integral number of counts for each individual counter is also stored in the data file and can be used in the data analysis.

2.3 Detection of positrons and muons

Typical positron detections are reported in Fig. 12. At $\mu_0 H = 0$ T the signals have a well-defined amplitude band, with the most probable pulse height value at ~ 350 mV. This is about 90 times the pulse height of the 1e-signals and 12 times the minimum threshold required to suppress the noise from the thermally generated charge carries to less than 100 counts per second. The most probable amplitude (charge) of the positron signals corresponds to ~ 130 fired cells. As the magnetic field increases, higher amplitudes appear in the signal spectrum: positrons, now moving on helical trajectories, travel longer paths and therefore deposit more energy in the counters. The amplitude of the 1e-signals at $\mu_0 H = 4.5$ T is about the same (within 10 %) as that at zero magnetic field implying that neither the G-APD nor the amplifier gain are influenced by the field.

The signals from the muon counter are shown in Fig. 13. Their most probable amplitude corresponds to about 16 fired cells (the pulse height is about 12 times that of the 1e-signals). Although the muon signals are a factor of 8 smaller in amplitude compared to that from positrons, they are still well above the noise level and can be detected with an efficiency close to 100 %. The amplitudes of the muon and 1e - signals practically do not depend on the magnetic field up to 4.5 Tesla. There is also no change of the muon signal amplitude up to an event rate of 3.6 MHz. Such excellent rate capabilities of the counter reflect the very short recovery time of the used G-APD.

The rate capabilities of a positron counter, see Fig. 14, were measured using a 28 MeV/c positron beam with the counter positioned perpendicular to the beam. The positron beam was obtained by tuning the separator, its intensity was varied by a slit system in the beamline. It was observed that the positron counter is capable to handle rather high event rates: for example, at 1 MHz the decrease of the signal amplitude is 25 %. In normal operating conditions positron rates are less than 200 kHz per counter.

2.4 ALC spectra

The good performance of an individual positron counter is a necessary but not sufficient condition for a proper performance of the ALC detector as a whole. Another crucial point is the role played by the detector configuration in high magnetic fields. The parameters of the detector layout (Fig. 2b) have been optimized by using GEANT4 simulations. Figure 15 shows a reasonable agreement between the data measured on 1 mm and 3 mm thick Cu samples and the behavior predicted by the simulations.

Figure 16 shows an example of the experimental data taken with the new detector system on a test sample giving ALC resonances at $\mu_0 H \approx 2$ T and 2.8 T. One full field range scan with a coarse step and two short range scans over the resonances using finer steps are reported. Note the exact reproducibility of the asymmetry baseline in these three scans indicating the overall *high stability* of the detector performance. Figure 17 exhibits the same data in the narrow field ranges around the resonances after subtraction of a straight baseline. A practically linear slope of the asymmetry baseline in a wide field range does not introduce any uncertainty in the line-shape analysis of the resonances.

Summary

The potential of the G-APD based detector technology for μSR has been demonstrated by building a detector system for the 5 Tesla ALC spectrometer (see Fig. 18). The new ALC detector is compact, insensitive to the magnetic field and is operated at a voltage below 50 Volts. It shows stable and reliable performance and delivers good quality ALC spectra. The performance predicted by the GEANT4 simulations is close to the measured one.

The new detector setup allows us to proceed with the upgrade of the cryogenic part of the spectrometer, which will be done as the next step.

Acknowledgements

One of the authors, A.S., expresses his gratitude to Dr. D. Renker (PSI) and Dr. Yu. Musienko (Northeastern University, Boston) for consultations on G-APDs, and U. Greuter (PSI) for help with the amplifier design.

We are indebted to Photonique SA (Switzerland) for providing G-APDs (Solid State PhotoMultipliers) of outstanding performance.

This project has been supported by the European Commission under the 6th Framework Programme through the Key Action: Strengthening the European Research Area, Research Infrastructures. Contract no.: RII3-CT-2003-505925.

References

[1] `http://lmu.web.psi.ch/facilities/alc/alc.html`

[2] The application of the ALC technique was first proposed in:
A. Abragam, *C. R. Acad. Sc. Paris* 299, Series II, no. 3 (1984) 95.
A detailed description and applications can be found, for example, in:
R.F. Kiefl and S.R. Kreitzman, *Perspectives of Meson Science*, Ch. 9, Eds.: T. Yamazaki, K. Nakai and K. Nagamine, Elsevier Science Publ. B.V. (1992); and in:
E. Roduner, Chem. Soc. Rev. 22 (1993) 337.

[3] A. Stoykov *et al.*, Nucl. Instr. and Meth. A 550 (2005) 212.

[4] S. Agostinelli *et al.*, Nucl. Instr. and Meth. A 506 (2003) 250-303.

[5] J. Allison *et al.*, IEEE Trans. on Nuclear Science 53, n. 1 (2006) 270-278.

[6] R. Scheuermann *et al.*, Nucl. Instr. and Meth. A 581 (2007) 443.

[7] A voltage regulator module PHV8-600VLC for biasing avalanche photodiodes has been developed at PSI by S. Ritt and R. Schmidt. The module houses 8 channels and is controlled via the MSCB interface. For each channel the voltage can be set in the range $2 - 600$ V with the resolution of 16 bits; the channel current is measured with the resolution of 1 nA.

[8] `http://www.photonique.ch`

[9] `http://www.hamamatsu.com`

[10] V.V. Zhuk, A.V. Stoykov, R. Scheuermann, PSI TM-35-05-01 (2005) 1-7.

[11] Yu. Musienko *et al.*, PoS (PD07) 012; `http://pos.sissa.it`

[12] H. Oide *et al.*, PoS (PD07) 008; `http://pos.sissa.it`

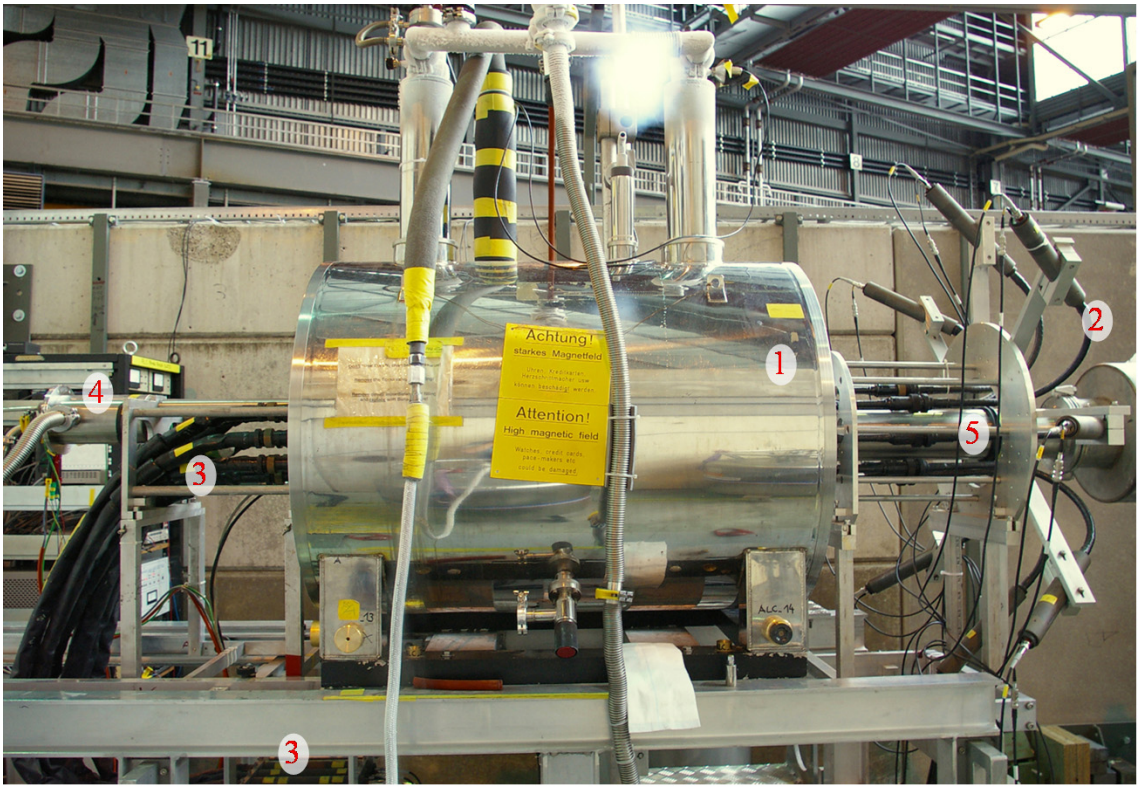

Figure 1: ALC spectrometer equipped with the "old" PMT-based detector system in the πE3 experimental area of SμS. Numbers indicate: 1 – superconducting solenoid (length 1 m, warm bore diameter 20 cm, maximum field 5 T); 2 – backward positron detector (8 segments, visible are light guides and PMTs); 3 – forward detector (7 segments, visible are flexible light guides (fiber bundles) and PMTs); 4 – cryostat; 5 – beamline extension tube (the nose).

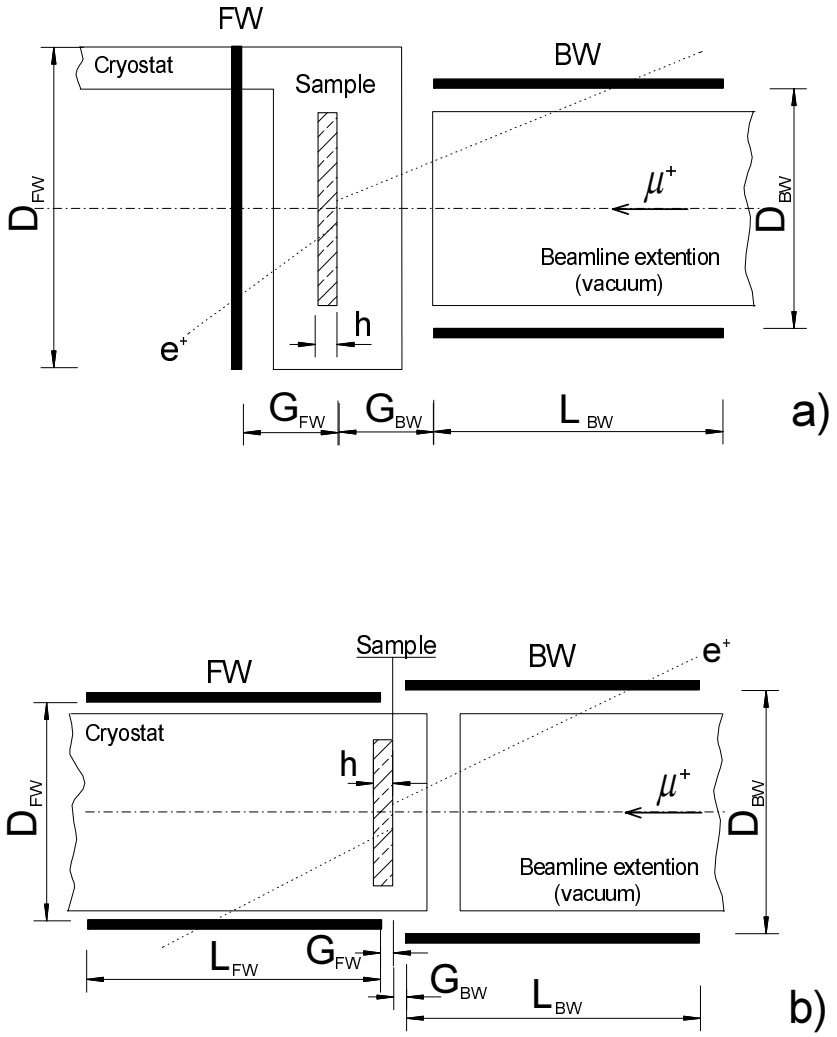

Figure 2: Two basic arrangements of positron detectors in an ALC experiment: a) a ring-shaped BW detector co-axial with the beam, and a disc-shaped FW detector normal to the beam; b) a two-ring detector setup.

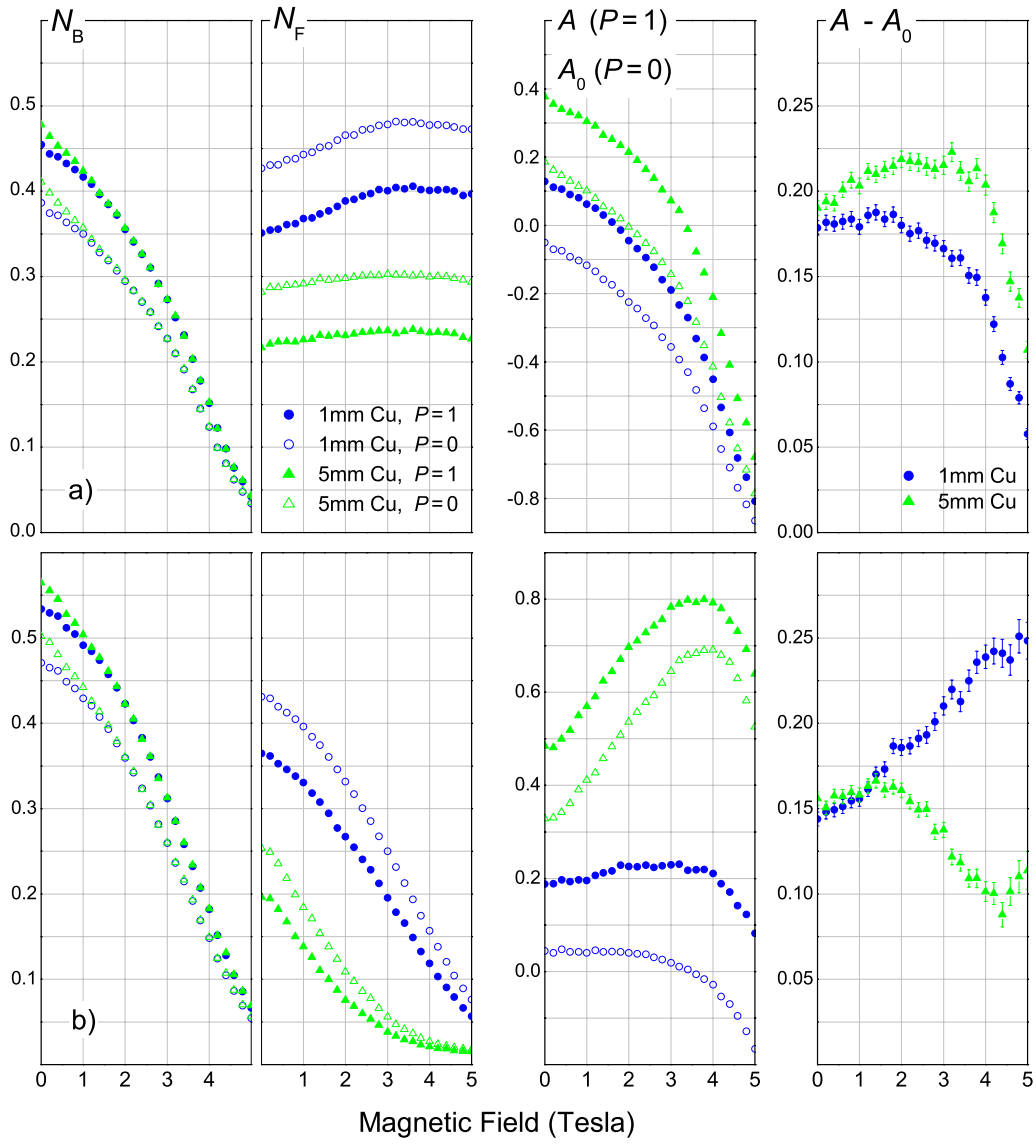

Figure 3: GEANT4 simulations for the detector geometries shown in Figure 2a (a) and Figure 2b (b). $N_{\rm B}$ and $N_{\rm F}$ are integral counts in BW and FW detectors normalized to the number N_μ of incoming muons. Filled symbols refer to the polarized muon beam $P = 1$, while open symbols refer to a beam with $P = 0$ (the non-polarized muon beam was simulated as a composition of two beams with $P = 1$ and $P = -1$). Note that the values of $N_{\rm B}$ and $N_{\rm F}$ for $P = 0$ give the effective solid angle of the detectors. The effective solid angle of the ring-shaped detectors is gradually decreasing with increasing the field H (as the field increases more and more positrons are confined in spiral trajectories with diameter smaller than that of the detector ring and thus cannot reach the detector). The asymmetries A and A_0 correspond to the polarized and non-polarized beam respectively (only A is measured in the experiment). The maximum possible change of the asymmetry is given by the difference $A - A_0$. The parameters used in the simulations are: a) $D_{\rm BW} = 120$ mm, $D_{\rm FW} = 180$ mm, $L_{\rm BW} = 300$ mm, $G_{\rm BW} = G_{\rm FW} = 20$ mm; b) $D_{\rm BW} = 110$ mm, $D_{\rm FW} = 94$ mm, $L_{\rm BW} = L_{\rm FW} = 120$ mm, $G_{\rm BW} = G_{\rm FW} = 2$ mm. The sample is a copper plate 1 mm or 5 mm thick; the detectors are non-segmented; the whole setup is in vacuum; the muon beam momentum is 29.8 MeV/c; beamline extension tube and the cryostat are not included in the GEANT4 model.

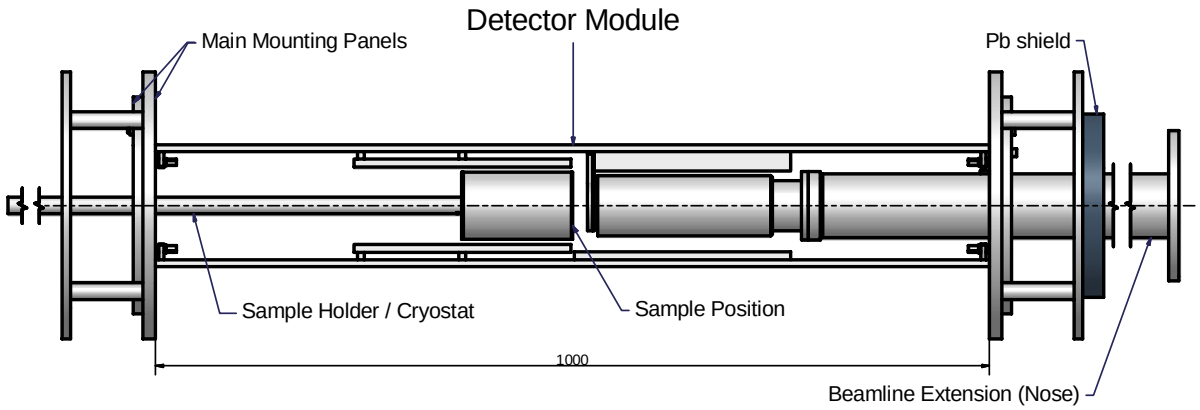

Figure 4: Mounting of the detector module in the warm bore of the solenoid (the solenoid is not shown). Design view. Muon beam comes from the right.

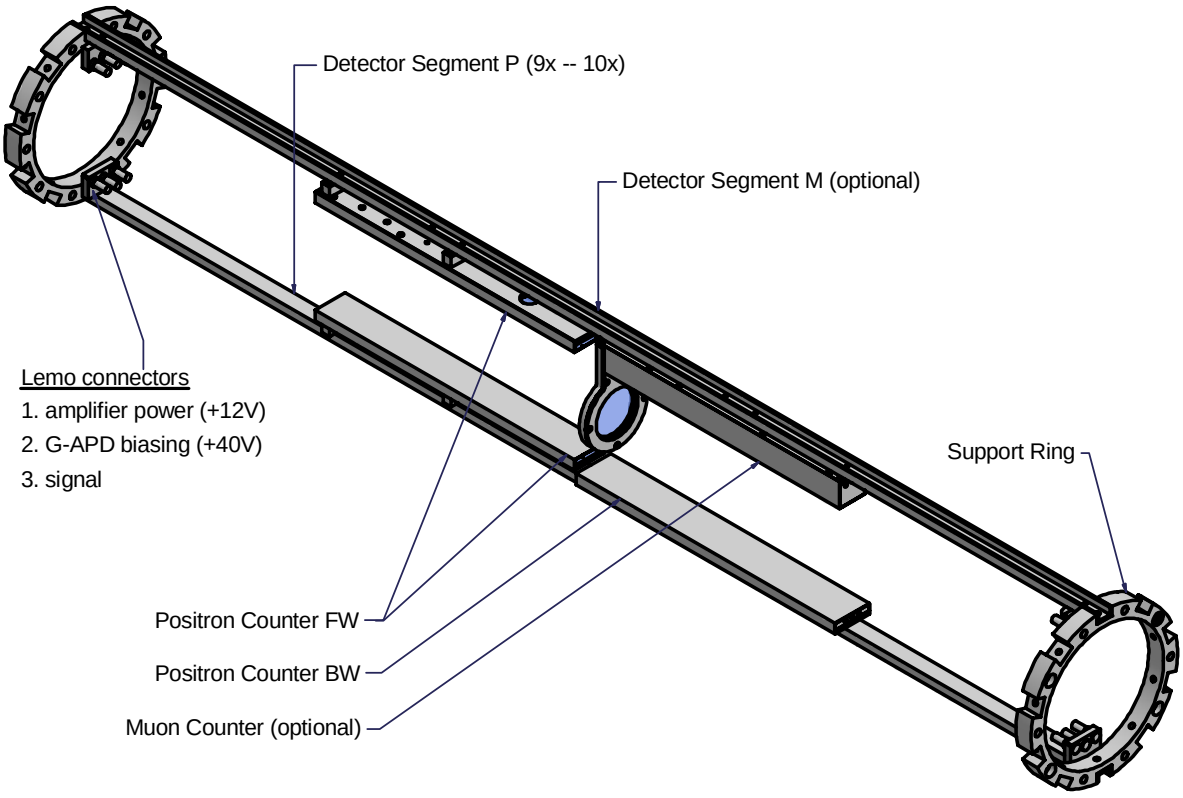

Figure 5: Detector module – design view. Only two out of ten detector segments are shown.

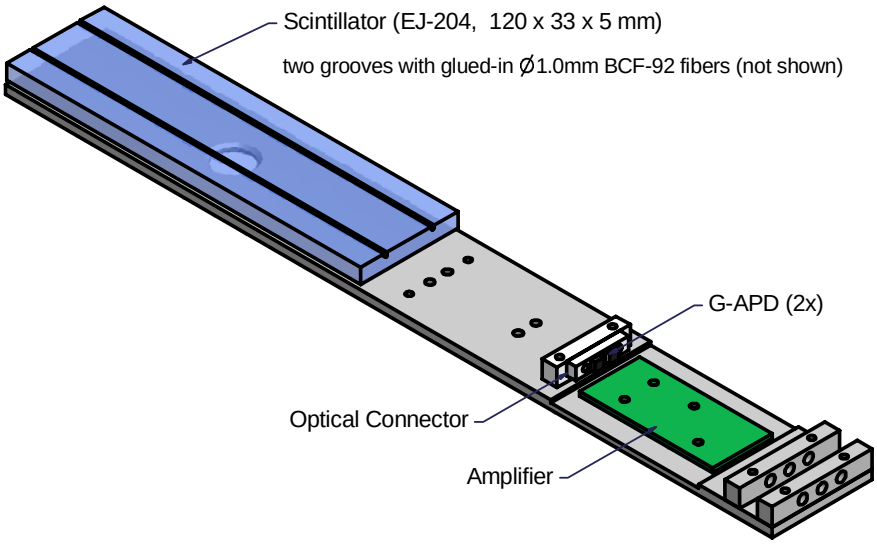

Figure 6: BW positron counter. Design view.

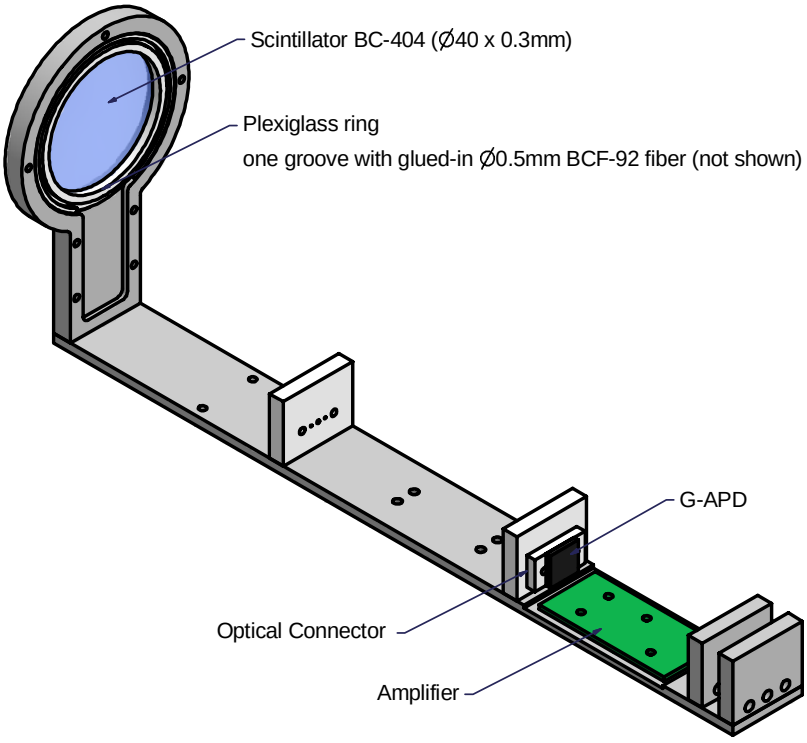

Figure 7: Muon counter. Design view.

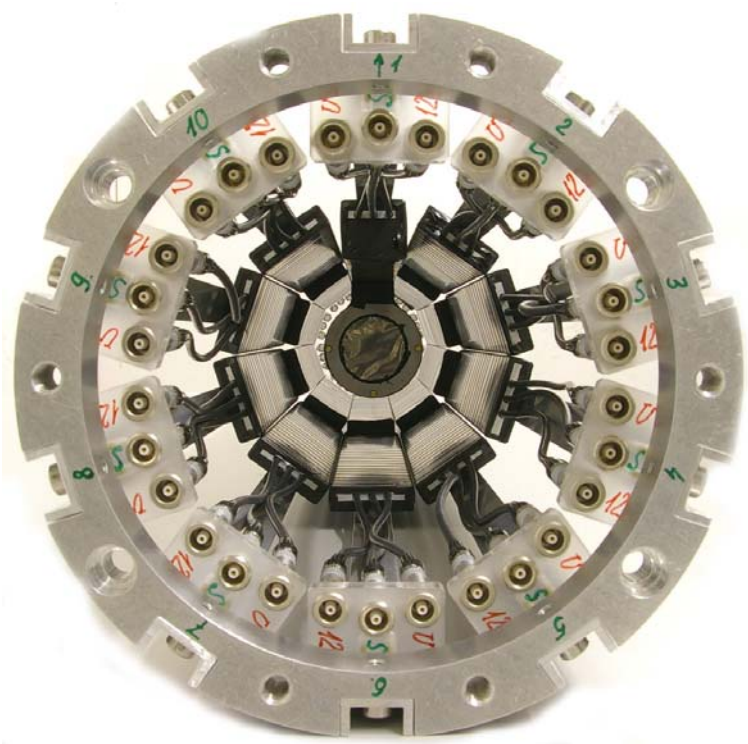

Figure 8: Detector module in assembly. View along the direction of the muon beam.

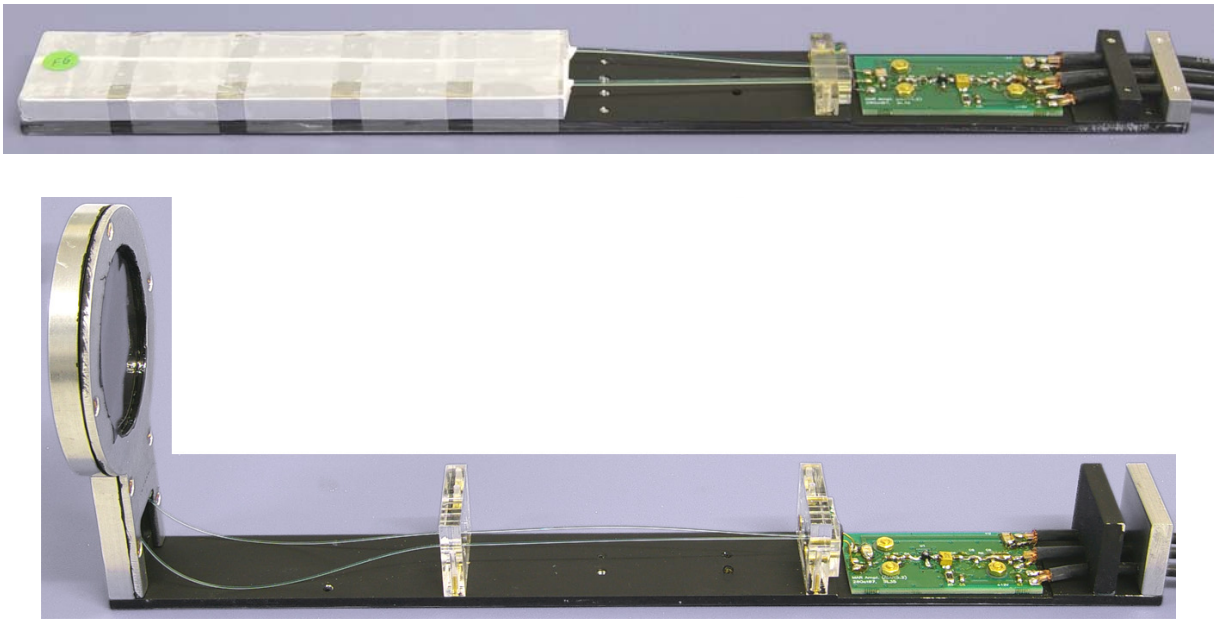

Figure 9: Positron and muon counters. The lids for mechanical protection and the black tape wrapping for light protection have been removed.

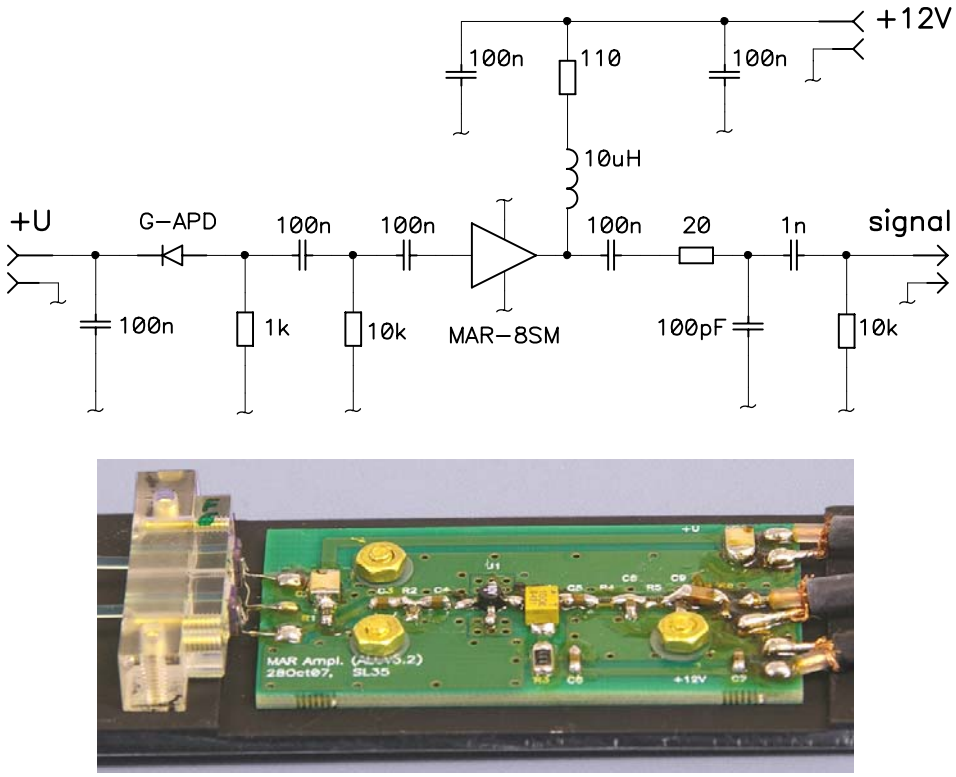

Figure 10: The scheme and the board of the amplifier (gain ~ 20, bandwidth ~ 70 MHz). The same amplifier is used in both positron and muon counters.

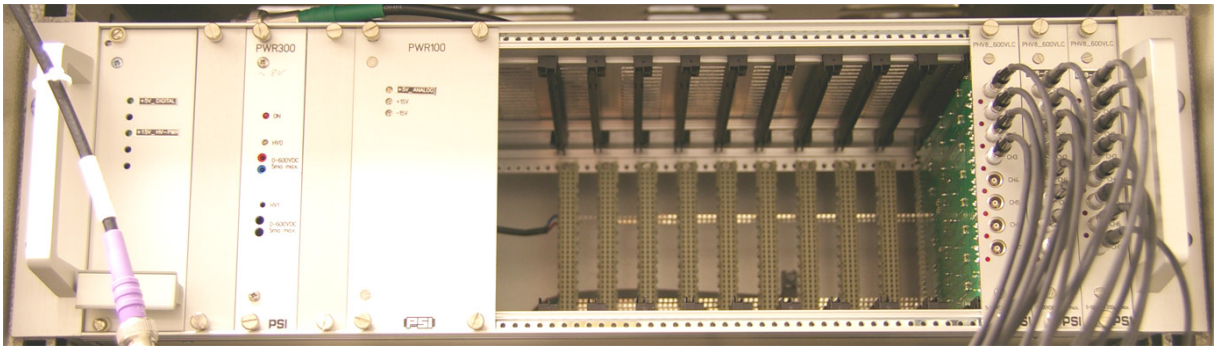

Figure 11: A crate with 3 voltage regulator modules PHV8-600VLC for biasing avalanche photodiodes (right-hand side). Each module houses 8 channels and is controlled via the MSCB - interface. The channel voltage can be set in the range $2-600$ V with the resolution of 16 bits; the channel current is measured with the resolution of 1 nA.

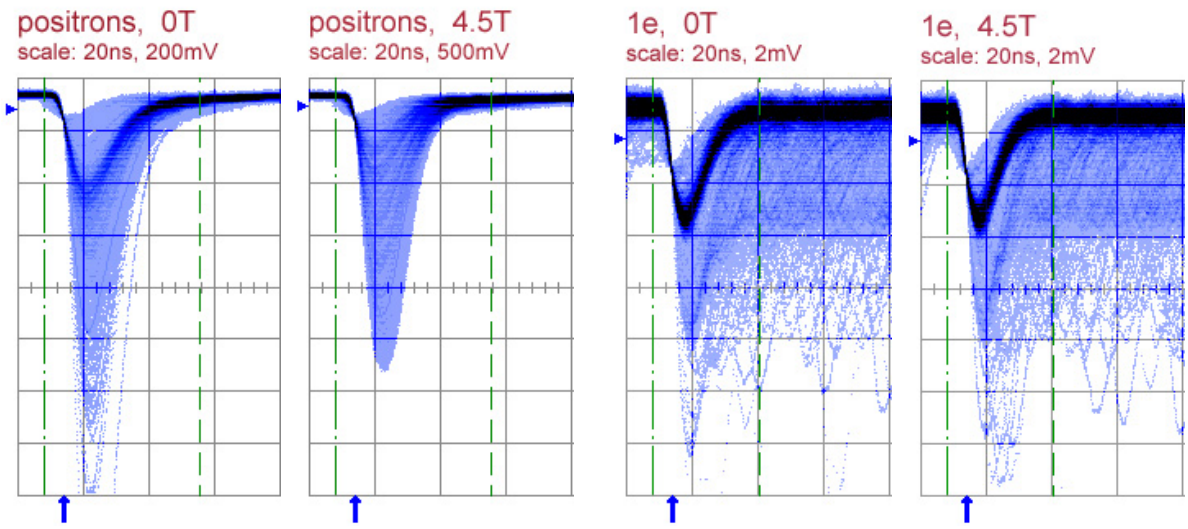

Figure 12: Detection of *positrons* in one of the BW counters and its 1e - signals both in presence of 4.5 T magnetic field and in zero field. Note the different vertical scales.

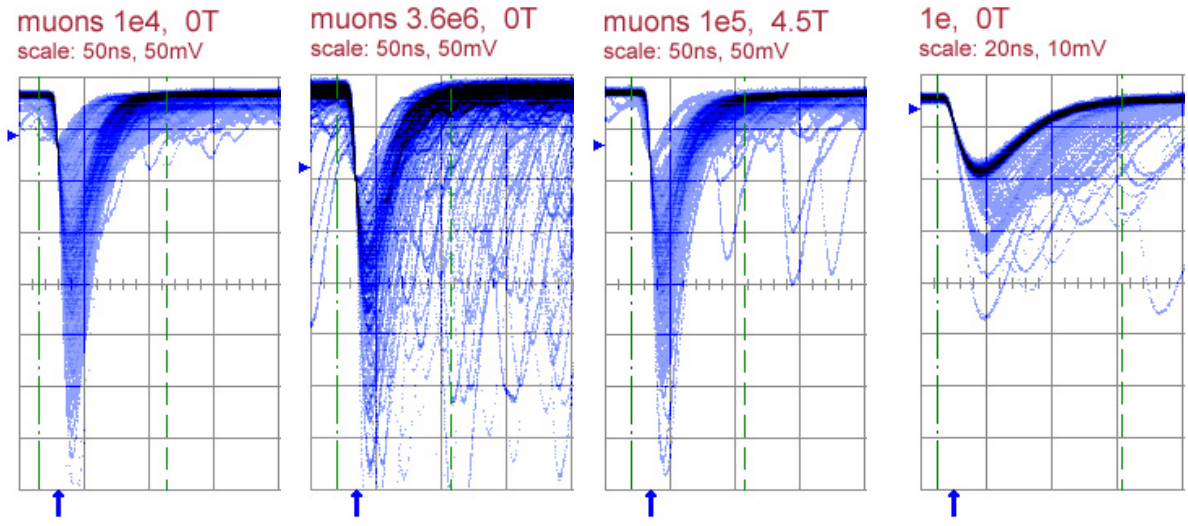

Figure 13: Detection of *muons* at different event rates ($10^4 - 3.6 \cdot 10^6$ s^{-1}) and magnetic fields (0 T and 4.5 T). Also shown are the 1e-signals.

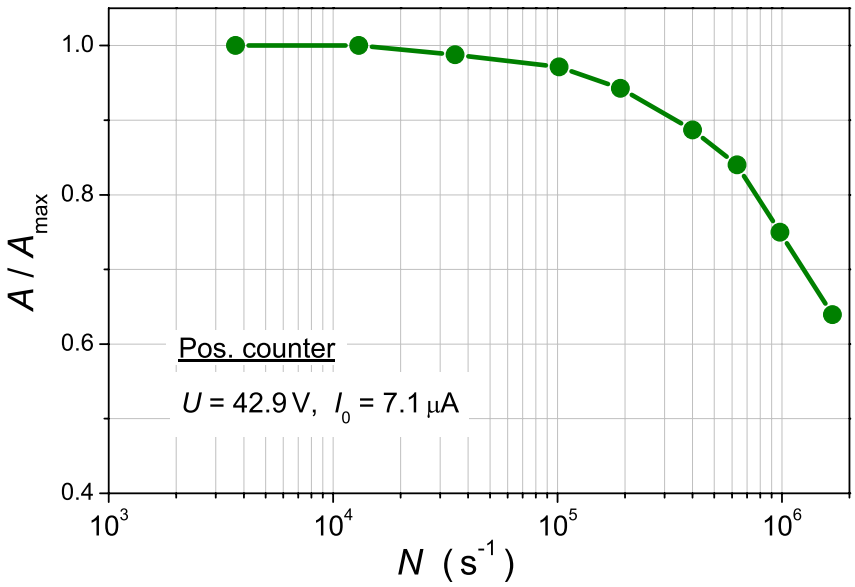

Figure 14: Rate dependence of the signal amplitude for one of the positron counters. The measurement is done with a 28 MeV/c positron beam with the counter normal to the beam. The line is drawn to guide the eye.

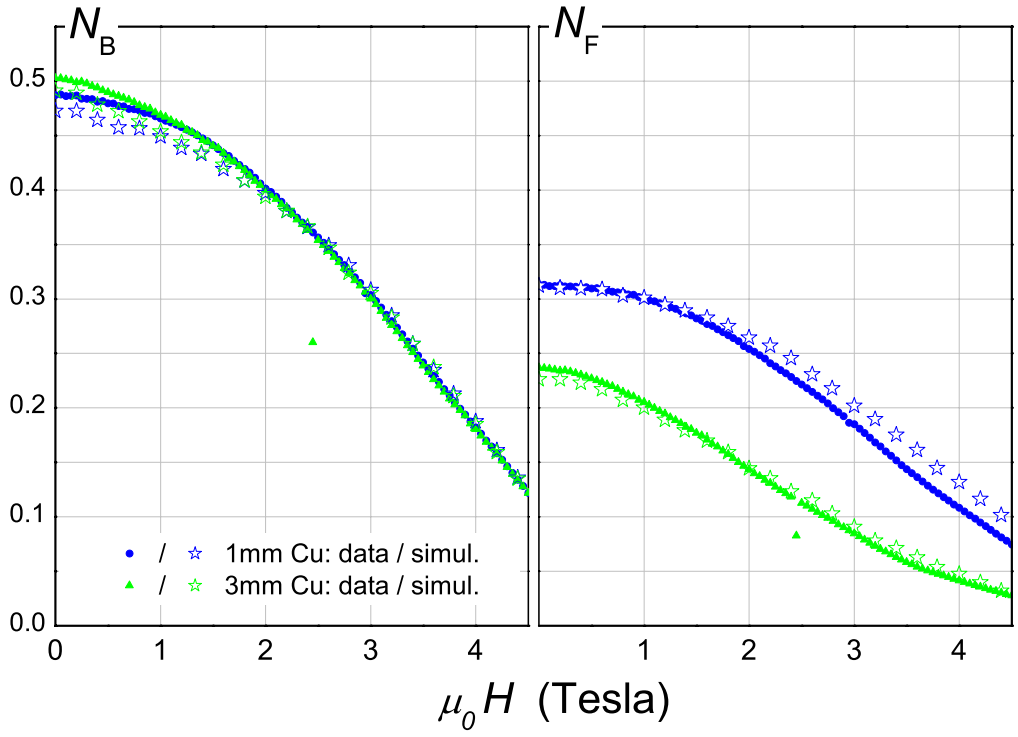

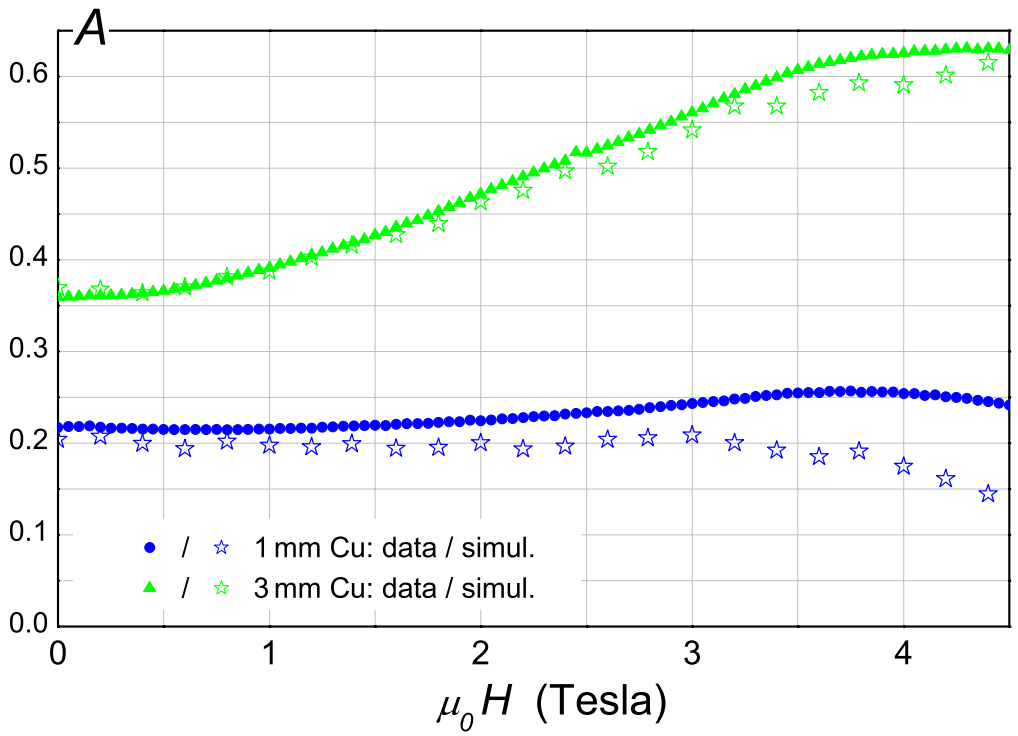

Figure 15: ALC spectra measured with the new detector on 1 mm and 3 mm thick Cu-samples vs. the predictions obtained using GEANT4 simulations. The measured integral counts N_B and N_F are normalized using a somewhat arbitrary, but realistic, value of the muon rate $N_\mu = 2.22 \cdot 10^6$ s^{-1}.

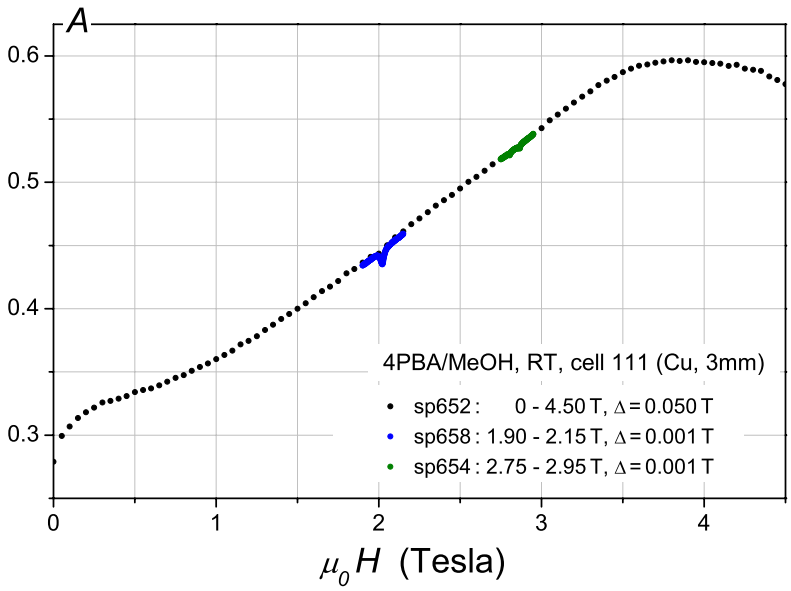

Figure 16: ALC spectra taken on a 4PBA/MeOH (4-phenylbutyrate/methanol) sample at room temperature: one wide field range scan and two short range scans over the resonances at around 2 T and 2.8 T. The sample cell is made of brass, the thickness of its rear wall is 3 mm.

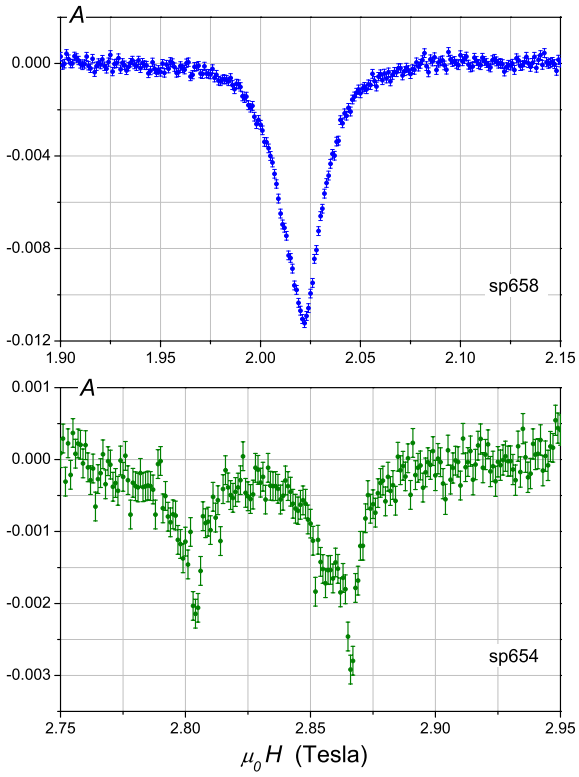

Figure 17: The same spectra (sp658 and sp654) as in Fig. 16 after the subtraction of a straight baseline.

Figure 18: ALC spectrometer equipped with the new G-APD based detector system in the experimental area πE3 of SμS: 1 – solenoid; 2, 3 – connecting cables (the detector module is inside the solenoid warm bore and not visible); 4 – sample holder; 5 – beamline extension tube.